W. PIEKARSKA*,#

MODELLING AND ANALYSIS OF PHASE TRANSFORMATIONS AND STRESSES IN LASER WELDING PROCESS

MODELOWANIE I ANALIZA PRZEMIAN FAZOWYCH I NAPRĘŻEŃ W PROCESIE SPAWANIA LASEROWEGO

The work concerns the numerical modelling of structural composition and stress state in steel elements welded by a laser beam. The temperature field in butt welded joint is obtained from the solution of heat transfer equation with convective term. The heat source model is developed. Latent heat of solid-liquid and liquid-gas transformations as well as latent heats of phase transformations in solid state are taken into account in the algorithm of thermal phenomena. The kinetics of phase transformations in the solid state and volume fractions of formed structures are determined using classical formulas as well as Continuous-Heating-Transformation (CHT) diagram and Continuous-Cooling-Transformation (CCT) diagram during welding. Models of phase transformations take into account the influence of thermal cycle parameters on the kinetics of phase transformations during welding. Temporary and residual stress is obtained on the basis of the solution of mechanical equilibrium equations in a rate form. Plastic strain is determined using non-isothermal plastic flow with isotropic reinforcement, obeying Huber-Misses plasticity condition. In addition to thermal and plastic strains, the model takes into account structural strain and transformation plasticity. Changing with temperature and structural composition thermophysical parameters are included into constitutive relations. Results of the prediction of structural composition and stress state in laser butt weld joint are presented.

Keywords: Phase transformations, Laser welding, Strains, Stresses, Numerical simulations

Praca dotyczy modelowania numerycznego składu strukturalnego i stanu naprężenia w elementach stalowych spawanych wiązką promieniowania laserowego. Pole temperatury w doczołowym złączu spawanym otrzymano z rozwiązania równania przewodnictwa ciepła z członem konwekcyjnym. Podano model źródła ciepła, a w algorytmie zjawisk cieplnych uwzględniono ciepło przemiany ciało stałe-ciecz, ciepła przemian w stanie stałym oraz ciepło parowania. Kinetykę przemian fazowych w stanie stałym oraz ułamki objętościowe powstających struktur wyznaczano w oparciu o klasyczne równania i wykresy ciągłego nagrzewania CTP$_A$ i spawalniczy wykres ciągłego chłodzenia CTP$_c$-S. W modelu przemian fazowych uwzględniono wpływ parametrów cyklu cieplnego na kinetykę przemian fazowych podczas spawania. Naprężenia chwilowe i własne wyznaczono z rozwiązania równań równowagi mechanicznej w formie prędkościowej. W wyznaczaniu odkształceń plastycznych wykorzystano prawo nieizotermicznego plastycznego płynięcia ze wzmocnieniem izotropowym oraz warunkiem plastyczności Hubera-Misesa. W modelu uwzględniono, oprócz odkształceń termicznych i plastycznych, odkształcenia strukturalne i transformacyjne. W związkach konstytutywnych uwzględniono zmiany parametrów termofizycznych w funkcji temperatury i składu fazowego. Przedstawiono wyniki prognozowania składu strukturalnego i stanu naprężenia doczołowego połączenia spawanego laserowo.

1. Introduction

Laser beam welding generates the impact heating of the material and in consequence large temperature gradients, causing rapid changes in thermophysical properties of welded steel. In the heat affected zone (HAZ) the material is exposed to very different heating conditions. The resulting structure in HAZ depends on thermal cycle parameters such as: heating and cooling rates and the maximum temperature of thermal cycle. Temperature changes and phase transformations in solid state are the cause of a the formation of significant isotropic deformations, because structures arising during cooling process have greater specific volume than austenite structure.

Structural strain occurred in welded joint with thermal strain produce temporary and finally residual stress [1-7]. Stress state in the joint after welding process and the type of obtained structure significantly affect operational properties and the quality of welded constructions. Knowledge about the structural heterogeneity of welded joints and stress state caused by welding are important for the design of constructions, in terms of static and dynamic loads.

Study concerning the analysis of phenomena occurring during laser welding process follows trends of a comprehensive analysis of coupled thermomechanical phenomena (Fig 1). The analysis is performed in the field of experimental research as well as analytical and numerical modelling of physical phenomena [6-15].

* INSTITUTE OF MECHANICS AND MACHINE DESIGN FOUNDATIONS, CZESTOCHOWA UNIVERSITY OF TECHNOLOGY, DĄBROWSKIEGO 73, 42-200 CZĘSTOCHOWA

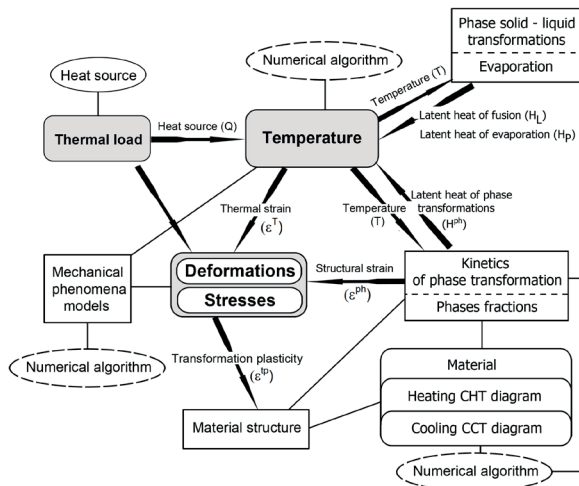# Corresponding author: piekarska@imipkm.pcz.pl

Fig. 1. Diagram of the correlation of basic physical phenomena occurring in laser welding of steel

An important issue in numerical simulations of welding process is a proper determination of thermal loads which determines the shape of the weld, its structure composition and properties, and in consequence stresses occurring in the joint. An important feature of laser beam as a heat source of high power and concentration is a deep penetration of welded material. This depth, as shown in the analysis of the process is closely related to the density of heat source power, the level of laser energy concentration and physical properties of the material. The local impact increase of temperature leads not only to material melting, but also leads to the local evaporation of metal. The effect of laser material heating depends on the assumed model of heat source power distribution used in the numerical analysis and the mechanism of metal melting [13-16]. Thermophysical properties varying with temperature as well as latent heats associated with solid-liquid, liquid-gas transformations and latent heats of phase transformations in solid state are taken into account in the model due to the wide range of temperatures present in laser welding process.

The analysis of phase transformations in solid state during welding is focused mainly on phase transformations during cooling process. The analysis of the kinetics of phase transformation is carried out using mathematical models that are well known in the literature and CCT diagrams. The analysis of phase transformations in heating process in most cases is carried out for constant Ac_1 and Ac_3 temperatures. The influence of maximum heating temperature is generally ignored. High heating rates as well as very high and various maximum heating temperatures of steel occur in the case of welding process using highly concentrated heat source of a high power like a laser beam heat source [17-24]. These factors affect the kinetics of phase transformation in the solid state. Therefore, the influence of heating and cooling rates, and the impact of maximum temperatures of the thermal cycles on the kinetics of phase transformations during welding should be taken into account in numerical simulations of phase transformations in solid state [25-28]. Considering above facts, this work presents the analysis of the kinetics of phase transformations in welding using a high-speed and high-power heat source. Mathematical and numerical models of

phase transformations as well as modified numerical models of the prediction of structure composition in welded joints are developed on the basis of literature data and experimental research. Elastic-plastic material is assumed in the model of mechanical phenomena, taking into account plastic, thermal and structural strain as well as transformation plasticity [29-32]. Temporary and residual stress in welded joints are obtained on the basis of the solution of equilibrium equations in a rate form, which allows to consider thermophysical properties changing with temperature and phase composition in every increase of load.

An example of the prediction of temperature field, structure composition and stress state in laser butt-welded joint made of S460 steel are shown. Presented results of simulations are obtained on the basis of developed mathematical and numerical models implemented into author's computer solvers.

2. Thermal phenomena

Temperature field in elements welded by a movable heat source are determined by the solution of transient heat transfer equation with convective term, expressed as follows:

$$\nabla \cdot (\lambda \nabla T) = C_{ef}\left(\frac{\partial T}{\partial t} + \nabla T \cdot \mathbf{v}\right) - \widetilde{Q} \qquad (1)$$

where $\lambda = \lambda(T)$ is thermal conductivity dependent on temperature, C_{ef} is effective heat capacity, $\widetilde{Q}$ is a volumetric heat source and $\mathbf{v} = \mathbf{v}(x,y,z,t)$ is a vector determined by welding speed, $T(x,y,z,t)$ is a temperature and t is time.

Equation (1) is completed by initial condition $t = 0 : T = T_0$ and boundary conditions. Boundary conditions assumed in the analysis consist of Dirichlet, Neumann and Newton type conditions, with a heat loss due to convection and radiation taken into account. Generally, boundary conditions are expressed in the following formula:

$$-\lambda \frac{\partial T}{\partial n} = -q + \alpha(T|_\Gamma - T_0) + \varepsilon\sigma(T^4 - T_0^4) \qquad (2)$$

where α is a convective coefficient (assumed as average value $\alpha = 50$ W/m²K), $\varepsilon = 0.5$ is a radiation coefficient, σ is Stefan-Boltzmann constant and $q = q(r)$ is the heat flux towards the top surface of welded workpiece ($z=0$) in the source activity zone, $T_0 = 293$ K is an ambient temperature.

A volumetric heat source model is assumed with changing source power density along material penetration depth expressed as follows [15]:

$$Q(r,z) = \frac{\eta Q_L}{V}\exp\left[\left(1 - \frac{r^2}{r_z^2}\right)\left(1 - \frac{z}{d}\right)\right] \qquad (3)$$

where Q_L is a laser beam power [W], η is efficiency, d is a total penetration depth, $r = \sqrt{x^2 + y^2}$ is a current beam radius [m] and $z \in [0; \alpha_z d]$ is a current penetration [m], $V = \pi d\left(r_{\alpha z}^2\left(1 - \frac{2}{3}\alpha_z\right) + \frac{1}{3}\alpha_z(r_0^2 + r_0 r_{\alpha z})\right)$ is a volume of the

heat source [m^3], r_z is a total laser beam radius along penetration direction [m], defined as: $r_z = r(z) = r_0 - (r_0 - r_{az})\dfrac{z}{\alpha_z d}$, where r_0 is a radius of laser beam spot at the top surface of the workpiece ($z=0$) and r_{az} is a radius of the beam at the deep of penetration $z = \alpha_z d$, $\alpha_z \in [0;1]$ is experimentally defined coefficient depending on the welding speed.

Changing with temperature thermal conductivity is assumed in the model (Fig. 2). In solid state $\lambda = \lambda(T)$ is defined according to data form the literature [23]. Much higher value of $\lambda(T)$ is assumed at high temperatures, which corresponds to the motion of liquid material in the welding pool.

Latent heat of fusion, evaporation and latent heat of phase transformations in solid state [33-35] are considered in the work. Between solidus and liquidus temperatures $T \in [T_S; T_L]$ (solid-liquid transformation) the latent heat of fusion is taken into account, assuming linear increase of a solid fraction in the mushy zone [35]:

$$C_{\mathrm{ef}}(T) = \rho_{SL} c_{SL} + \rho_S \frac{H_L}{T_L - T_S} \quad \text{for } T \in [T_S; T_L] \quad (4)$$

where H_L [J/kg] is the latent heat of fusion and the product of density and specific heat in the mushy zone equals:
$c_{SL} \rho_{SL} = c_S \rho_S (1 - f_L) + c_L \rho_L (f_L)$.

The latent heat of evaporation is considered in temperatures exceeding the boiling point of steel (T_b). The effective heat capacity for $T \geq T_b$ is expressed as follows:

$$C_{\mathrm{ef}}(T) = \rho_L c_L + \frac{\rho_L H_b}{T_{\max} - T_b} \quad \text{for } T \geq T_b \quad (5)$$

where H_b [J/kg] is latent heat of evaporation, $T_{\max}$ is a maximum temperature.

Heats generated during transformation of austenite into ferrite, pearlite, bainite and martensite are included into the effective heat capacity. Effective heat capacity during phase transformations in solid state is defined assuming the approximation with the increase of a volumetric fraction of i-th phase in the solid state (latent heats of austenite into ferrite $H_{A \to F}$, pearlite $H_{A \to P}$, bainite $H_{A \to B}$ and martensite $H_{A \to M}$ transformation).

$$C(T) = \begin{cases} \rho_S c_S + \sum_i \rho_S H_i \dfrac{d\eta_i(T)}{dT} & \text{for } T \in [T_s^i; T_f^i] \\ \rho_S c_S & \text{for } T \notin (T_s^i; T_f^i) \end{cases} \quad (6)$$

where T_s^i and T_f^i are start and final temperatures of each phase transformation (H_i) is a latent heat of i-th phase transformation.

Latent heats of transformation (H_i) of austenite into ferrite, pearlite, bainite and martensite in welded low carbon steel (according to author of [33,34] are approximated by the following square functions for temperatures given in °C):

$$H_{A \to F}(T) = -0.50315T^2 + 388.32T + 39652$$
$$H_{A \to P}(T) = -0.42990T^2 + 283.51T + 86588$$
$$H_{A \to B}(T) = -0.40676T^2 + 264.28T + 86860 \quad (7)$$
$$H_{A \to M}(T) = H_{A \to B}(T)$$

Effective heat capacity in solid state for chosen exemplary thermal cycles (for two chosen cooling rates v_c=70 K/s and v_c=111 K/s) is shown in Fig. 3.
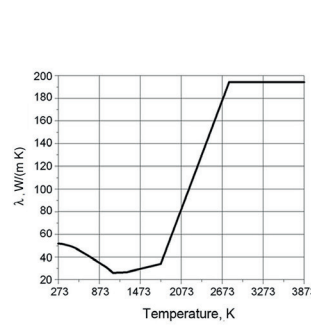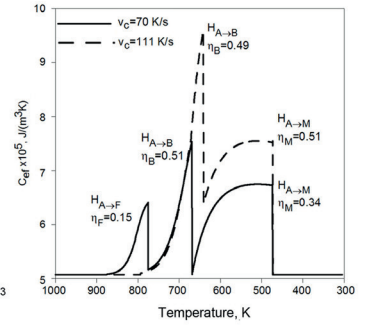

Fig. 2. Thermal conductivity assumed in calculations

Fig. 3. Effective heat capacity for two chosen cooling rates

Heat transfer equation (1) is numerically solved using finite difference method (FDM) in forward Euler's time integration scheme. For the stabilization of solution algorithms Péclet number is implemented directly into central difference quotients.

3. Phase transformations in solid state

The kinetics of austenite is described on the basis of Johnson-Mehl-Avrami (JMA) equations or modified Koistinen-Marburger (KM) equation [36, 37].

$$\tilde{\eta}_A(T, t) = 1 - \exp(-b t^n) \quad (8)$$

$$\tilde{\eta}_A(T, t) = 1 - \exp(-k(T_{sA} - T)) \quad \text{for } T \geq 500\,K/s \quad (9)$$

where $b = b(T) = -\dfrac{\ln(\eta_f)}{(t_s)^{n(T)}}$, $n = n(T) = \dfrac{\ln\left(\ln(\eta_s)/\ln(\eta_f)\right)}{\ln(t_s/t_f)}$ are based on start (η_s=0.01) and finish (η_f=0.99) conditions of phase transformation, t is time, $t_s = t_s(T_{sA})$ and $t_f = t_f(T_{fA})$ are start and finish times of phase transformation respectively, whereas T_{sA} and T_{fA} are start and finish temperatures of this phase transformations and coefficient $k = -\dfrac{\ln(0.01)}{T_{sA} - T_{fA}}$

The case of incomplete austenitization is considered if maximum temperature of thermal cycle is found in the range $[Ac_1 \div Ac_3]$. The maximum fraction of austenite during welding

is calculated as: $\tilde{\eta}_A = (T_{max} - Ac_1(t) / (Ac_3(t) - Ac_1(t))$. In this case, fractions of every phase during cooling is assumed to be a sum of fraction transformed from austenite during cooling process and remaining rest of this phase untransformed into austenite during heating process.

Fractions of phases arising from austenite during cooling process are determined by temperature and cooling rate $v_{8/5}$ in temperature range [800÷500]°C. A fraction of a new phase like bainite, ferrite and pearlite (diffusive transformations) are determined using JMA formula, taking into account existing within it phases. Volumetric fraction of martensite appearing below M_S temperature is calculated using modified KM formula:

$$\eta_{(\cdot)}(T,t) = \eta_{(\cdot)}^{\%} \tilde{\eta}_A \left(1 - \exp\left(-b\left(t(T)\right)^n \right) \right) \qquad (10)$$

$$\eta_M(T) = \eta_{(\cdot)}^{\%} \tilde{\eta}_A \left(1 - \exp\left(-k\left(\frac{M_s - T}{M_s - M_f} \right)^m \right) \right), \qquad (11)$$
$$T \in \left[M_s, M_f\left(v_{8/5} \right) \right]$$

where $\eta_{(\cdot)}^{\%}$ is a maximum phase fraction for given cooling rate, estimates using CCT diagram, $\tilde{\eta}_A = 1 - \sum_k \eta_k$, where η_k is a fraction of phase arisen previously in cooling process. Coefficients $b = b\left(T\left(v_{8/5}\right)\right)$ and $n = n\left(T\left(v_{8/5}\right)\right)$ are determined in the same way like for heating process, m and k are coefficients measured experimentally (m=1 and k=0,024 for investigated steel).

The increase of the isotropic strain caused by changes of the temperature ($d\varepsilon^T$) and phase transformations ($d\varepsilon^T$) during heating and cooling are calculated using following formula:

$$d\varepsilon^{TPh} =$$
$$d\varepsilon^T + d\varepsilon^{Ph} = \sum_i \alpha_i(T)\eta_i dT - sign(dT)\sum_i \varepsilon_i^{Ph}(T)d\eta_i \qquad (12)$$

where $sign(.)$ is a sign function, subscript stays for i=A, B, F, P and M, $\alpha_i(T)$ are coefficients of thermal expansion of: austenite, bainite, ferrite, martensite and pearlite, respectively, $\varepsilon_i^{Ph}(T)$ are linear isotropic strains that occur during transformation of a base structure (e.g. bainitic-ferritic structure) into austenite in heating process and its non-isothermal decomposition under overcooling conditions of steel (ferrite, pearlite, bainite and martensite).

In order to verify developed numerical models dilatometric tests are performed on dilatometer DIL805 B™hr Thermoanalyse GmbH for S460 steel with chemical composition given in Table 1. The study is performed for three austenitizing temperatures (1100, 1200 and 1300°C) with considered various heating and cooling rates for the proper analysis of the influence of important parameters of welding thermal cycle on the kinetics of phase transformations. CHT and CCT diagrams of S460 steel and final fractions of microstructure constituents are presented in Fig. 4.

TABLE 1

Chemical composition of the S460 steel [%]

C	Mn	Si	Cr	Ni	Cu	V	Al	Nb
0.19	1.62	0.60	0.10	0.09	0.11	0.10	0.032	0.012

Discrete CCT diagram model is applied on the basis of dilatometric research of S460 steel, taking into account the effect of austenitizing temperature on the offset of CCT diagram and thus the structure composition of steel. On the basis of determined CCT diagram offsets by parameters: Δt_B=0.3 s for bainite and Δt_F=1 s for ferrite (Fig. 4), the relative offset between CCT diagrams for different austenitizing temperatures in the range of 1000÷1300°C is specified using the following formulas:

$$t_B(T_{max}) = t_B(1100) + \Delta t_B(T_{max} - 1100) / 100$$
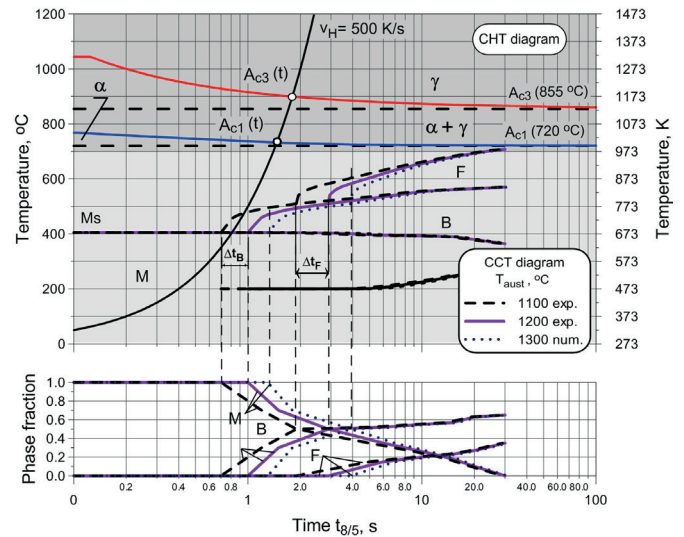$$t_F(T_{max}) = t_F(1100) + \Delta t_F(T_{max} - 1100) / 100 \qquad (13)$$

Fig. 4. CHT and CCT diagrams and final fractions of microstructure constituents for S460 steel

Testing numerical simulations are executed as a validation of developed models of phase transformations in solid state. Simulations results are verified on the basis of performed dilatometric research on analyzed steel. Simulated dilatometric curves determined for chosen heating and cooling parameters are compared to experimentally obtained curves.

Numerical calculations use mathematical models of phase transformations given in Eq. (8) – Eq. (12) as well as CHT and CCT diagrams for S460 steel. Volumetric fractions of phases are determined as well as the kinetics of phase transformations, thermal and structural strains. An example of dilatometric curve obtained for austenitic temperature 1200°C, heating rate v_H= 2600 K/s, cooling rate $v_{8/5}$= 20 K/s with corresponding kinetics of phase transformations is shown in Fig. 5.
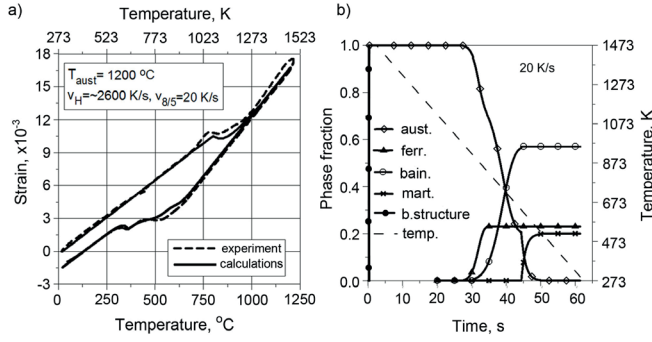
Fig. 5. Dilatometric curves a) and kinetics of phase transformations b) of S460 steel (vH = 2600 K/s and v8/5 = 20 K/s)

Values of thermal expansion coefficients $(\alpha_{(i)} = \alpha_{(i)}(T))$ of every structural constituent as well as isotropic structural strains $(\varepsilon_{(i)}^{ph})$ generated by phase transformations are determined on the basis of results of experimental verification. Values determined for S460 steel are presented in Table 2.

The coefficient of thermal expansion of the base structure of analyzed steel depends on temperature $\alpha_{bs} = \alpha_{bs}(T)$. The dependency of $\alpha_{bs}(T)$ coefficient in a function of temperature, which results from the comparison of experimental dilatometric curves with simulation results, is well described by square function, expressed as follows:

$$\alpha_{bs}(T) = -1.302 \times 10^{-11}T^2 + 2.149 \times 10^{-8} + 6.436 \times 10^{-6} \quad (14)$$

Values of coefficients are selected for a discrete α_{bs}, equal to 11.5, 15.0 and 15.0 ($\times 10^{-6}$) 1/K respectively at temperatures of 20, 600 and 720°C.

4. Mechanical phenomena

Equilibrium equations in a rate form approach are adopted in modelling of mechanical phenomena. This allows tracking thermo-physical properties changing with temperature and phase composition in every load increase [38, 39].

$$\nabla \circ \dot{\boldsymbol{\sigma}}(\mathbf{x}, t) = \mathbf{0}, \ \dot{\boldsymbol{\sigma}} = \dot{\boldsymbol{\sigma}}^T \quad (15)$$

where $\boldsymbol{\sigma} = \boldsymbol{\sigma}(\sigma_{\alpha\beta})$ is a stress tensor, symbol (°) means incomplete internal multiplication factor, $\mathbf{x} = \mathbf{x}(x_\alpha)$ represents a vector of the position of the particle (point).

Equations (15) are supplemented by constitutive relations based on the additive model of strains rate, expressed as follows:

$$\dot{\boldsymbol{\sigma}} = \mathbf{D} \circ \left(\dot{\boldsymbol{\varepsilon}} - \dot{\boldsymbol{\varepsilon}}^{Tph} - \dot{\boldsymbol{\varepsilon}}^p - \dot{\boldsymbol{\varepsilon}}^{tp}\right) + \dot{\mathbf{D}} \circ \boldsymbol{\varepsilon}^e \quad (16)$$

where: $\mathbf{D} = \mathbf{D}(T, \Sigma\eta_k)$ is a elasticity tensor dependent on temperature (T) and phase composition $(\Sigma\eta_k)$, $\boldsymbol{\varepsilon}^e$ represents an elasticity strains tensor, $\boldsymbol{\varepsilon}^{Tph}$ - isotropic tensor of thermal and structural strains, $\boldsymbol{\varepsilon}^p$ - plastic strains tensor, whereas $\boldsymbol{\varepsilon}^{tp}$ represents the tensor of transformation plasticity.

A linear dependence of thermal and physical parameters is assumed. The dependence is contained in material constant tensor ($\mathbf{D}$), for example Young's modulus (E) and tangential modulus (E^t) and the temperature and phase composition:

$$E\left(T, \sum\eta_k\right) = \sum E_k(T)\eta_k, E^t\left(T, \sum\eta_k\right) = \sum E_k^t(T)\eta_k,$$
$$k = 1, \ldots, 5 \quad (17)$$

Equilibrium equations (15) are also supplemented by initial conditions and boundary conditions. Initial conditions are expressed in the following form:

$$\boldsymbol{\sigma}(\mathbf{x}, t_0) = \boldsymbol{\sigma}_0(\mathbf{x}) = \mathbf{0}, \quad \boldsymbol{\varepsilon}^e(\mathbf{x}, t_0) = \boldsymbol{\varepsilon}_0(\mathbf{x}) = \mathbf{0} \quad (18)$$

Whereas, boundary conditions on the edge elements (Γ_u), where the degrees of freedom are reduced, i.e.:

$$\dot{\mathbf{U}}(\mathbf{x}, t)\Big|_{\Gamma_u} = \dot{\bar{\mathbf{U}}}, \ \left(\bar{\mathbf{U}}\Big|_{\Gamma_u} = \mathbf{0}\right) \quad (19)$$

where $\mathbf{U}$ is a displacement vector.

Plastic strains are determined using the theory of non-isothermal plastic flow associated with the Huber-Misses plasticity condition and isotropic strengthening. Thus, plastic flow functions ($f = f(\boldsymbol{\sigma}, Y)$) are adopted in the following form [30, 38]:

$$f = \sigma_{ef} - Y\left(T, \sum\eta_k, \varepsilon_{ef}^p\right) = 0, \quad (20)$$

where σ_{ef} represents an effective stress, ε_{ef}^p is an effective plastic strain, $Y = Y(T, \Sigma\eta_k, \varepsilon_{ef}^p)$ is a plasticized stress of material on the phase components $(\Sigma\eta_k)$ at a temperature T and effective plasticity strain (ε_{ef}^p).

Plasticized stress of material in a model of isotropic strengthening is determined by the following relationship:

$$Y\left(T, \sum\eta_k, \varepsilon_{ef}^p\right) = Y_0\left(T, \sum\eta_k\right) + Y_H\left(T, \sum\eta_k, \varepsilon_{ef}^p\right) \quad (21)$$

TABLE 2

Thermal expansion coefficients and structural strains

Structure constituent	Austenite	Ferrite	Pearlite	Bainite	Martensite
Thermal expansion coefficients, ´10-6 [1/K]	$\alpha_A = 22.0$	$\alpha_F = 14.7$	$\alpha_P = 14.0$	$\alpha_B = 13.5$	$\alpha_M = 12.0$
Strucural strains, ´10-3	$\varepsilon_A^{ph} = 2.7$	$\varepsilon_F^{ph} = 3.0$	$\varepsilon_P^{ph} = 3.0$	$\varepsilon_B^{ph} = 3.5$	$\varepsilon_M^{ph} = 5.2$

where $Y_0 = Y_0(T, \Sigma\eta_k)$ is a yield points, $Y_H\left(T, \sum\eta_k, \varepsilon_{ef}^p\right)$ represents the excess of plasticized stress over the yield points.

Taking into account: strengthening ($\kappa = \kappa(T, \Sigma\eta_k, \varepsilon_{ef}^p)$), thermal softening ($\kappa^T = \kappa^T(T, \Sigma\eta_k, \varepsilon_{ef}^p)$) and structural strengthening or softening ($\kappa^{\eta_r} = \kappa^\eta(T, \Sigma\eta_k, \varepsilon_{ef}^p)$), the rate of plasticized stress is calculated using the following equation:

$$\dot{Y}\left(T, \sum\eta_k, \varepsilon_{ef}^p\right) = \kappa\dot{\varepsilon}_{ef}^p + \kappa^T\dot{T} + \sum_k \kappa^{\eta_k}\dot{\eta}_k \qquad (22)$$

where

$$\begin{aligned}
\kappa &= \frac{\partial Y}{\partial\varepsilon_{ef}^p} = \frac{\partial Y_H\left(T, \sum\eta_k, \varepsilon_{ef}^p\right)}{\partial\varepsilon_{ef}^p} \\
\kappa^T &= \frac{\partial Y}{\partial T} = \frac{\partial Y_0\left(T, \sum\eta_k\right)}{\partial T} + \frac{\partial Y_H\left(T, \sum\eta_k, \varepsilon_{ef}^p\right)}{\partial T} \\
\kappa^{\eta_k} &= \frac{\partial Y}{\partial\eta_k} = \frac{\partial Y_0\left(T, \sum\eta_k\right)}{\partial\eta_k} + \frac{\partial Y_H\left(T, \sum\eta_k, \varepsilon_{ef}^p\right)}{\partial\eta_k}
\end{aligned} \qquad (23)$$

Plastic strains are determined by the associated theory of plastic flow [38]:

$$\dot{\boldsymbol{\varepsilon}}^p = \dot{\Lambda}\frac{\partial f}{\partial\boldsymbol{\sigma}}, \quad \dot{f} = 0, \quad f = 0 \qquad (24)$$

where Λ is a plasticity scalar multiplication factor ($\Lambda = \varepsilon_{ef}^p$).

Plastic strains resulting from (23) are calculated as follows:

$$\dot{\boldsymbol{\varepsilon}}^p = \dot{\Lambda}\frac{3\mathbf{S}}{2Y} \qquad (25)$$

where $\mathbf{S}$ represents a deviator of stress tensor ($\mathbf{S} = \boldsymbol{\sigma} - \mathbf{I}\sigma_{kk}/3$).

To investigate transformation plasticity, the modified Leblond equation is used in which a function decreasing the rate of transformation plasticity with the time of transformation is applied [29, 30]:

$$\dot{\boldsymbol{\varepsilon}}^{tp} = \begin{cases} 0, & \eta_k < 0.03 \\ -\dfrac{\mathbf{S}}{Y_1}\sum_{k=2}^{k=5}(1-\eta_k)K_{1k}\ln(\eta_k)\dot{\eta}_k, & \eta_k \geq 0.03 \end{cases} \qquad (26)$$

where $K_{1k} = 3\varepsilon_{1k}^{ph}$ are volumetric structural strains when the material is transformed from the initial phase „1" into k-phase, and Y_1 represents the yield points at the output phase (soft).

The problem is solved using finite element method (FEM) by solving the system of equations [38]:

$$[\mathbf{K}]\{\dot{\mathbf{U}}\} = \{\dot{\mathbf{R}}^{Tph}\} - \{\dot{\mathbf{R}}^e\} + \{\dot{\mathbf{R}}^{ptp}\} \qquad (27)$$

where $\mathbf{K}$ is the stiffness matrix, $\dot{\mathbf{U}}$ nodal displacement vector, $\dot{\mathbf{R}}^{Tph}$ nodal force vector deriving from thermal strains and structural strains (from phase transformations), $\dot{\mathbf{R}}^e$ is the nodal force vector from material constants with temperature,

and $\dot{\mathbf{R}}^{ptp}$ the nodal force vector from plastic strains and transformation plasticity.

After the solution of the system of equations (27), displacements, strains, and stresses are determined by integration after the time of the sought-after values, from the initial time $(t = t_0)$ to the current time (t):

$$\mathbf{U}(\mathbf{x}, t) = \int_{t_0}^t \dot{\mathbf{U}}(\mathbf{x}, \tau)d\tau, \ \ \boldsymbol{\varepsilon}(\mathbf{x}, t) = \int_{t_0}^t \dot{\boldsymbol{\varepsilon}}(\mathbf{x}, \tau)d\tau, \ \ \boldsymbol{\sigma}(\mathbf{x}, t) = \int_{t_0}^t \dot{\boldsymbol{\sigma}}(\mathbf{x}, \tau)d\tau$$

$$(28)$$

In an iterative process of evaluation of plastic strains, a modified Newton-Raphson algorithm is used [38]. At the end of every iterative process, the increment step (Δt) is determined by the conditions:

$$\left|\sigma_{ef} - Y\right| \leq \varepsilon^{his} \qquad (29)$$

where: $\varepsilon^{his} = 0.01 \times Y_0(T, \Sigma\eta_k)$ is adopted in numerical simulations.

5. Examples of numerical prediction of structure composition in welded joint

Numerical simulation of laser welding process as a three-dimensional problem is made for cuboid elements with dimensions 250×50×5 mm. Analyzed domain is considered as a half of the joint to the plane of symmetry and discretized by differential grid with constant spatial step 0.01 mm in x direction and linearly decreasing spatial step in y direction (Fig. 6b) from 0.05 mm in the heat source activity zone where large temperature gradients are present, up to 2 mm in lower temperatures. The following process parameters are assumed in computer simulations: laser beam power Q_L=3800 W, welding speed v=1.0 m/min, and remaining simulation parameters r_0=1.0 mm, r_{az}=0.4 mm and α_z=0,2. Numerical analysis is performed assuming laser welding without additional material (Fig. 6a) and perfect contact between joined sheets.
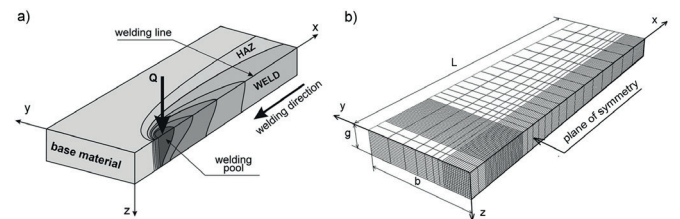

Fig. 6. Schematic sketch of considered system

Temperature field, calculated using presented models of thermal phenomena, is a basic factor for the prediction of structural composition as well as stress and strain states in welded butt-joint made of S460 steel. Young's modulus and tangential modulus (E and E^t) in the simulation of mechanical phenomena are temperature dependent, whereas yield strength (Y) depends on temperature and phase composition. Based on work presented in [39, 40] Young's modulus and tangential

modulus are set to 2×10^5 MPa and 2×10^4 MPa, yield strength 200 MPa, 320 MPa, 600 MPa, 1200 MPa and 320 MPa for austenite, ferrite, bainite, martensite and pearlite respectively in temperature 300 K. In temperatures $T\geq1700$ K Young's modulus and tangential modulus equal 100 MPa and 10 MPa, whereas yield strength equals 5 MPa. These values are approximated using square functions (Fig.7).
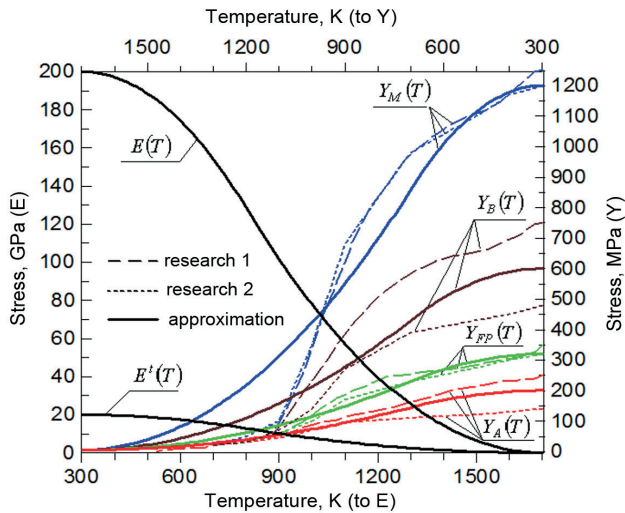
phase transformations and numerically determined structure composition at different depths of the joint (full austenitization) depend on both cooling rates and austenitizing temperature. All present differences partly result from varying cooling rates, but primarily due to the use of "dynamic" CCT diagrams in the numerical model (huge differences in austenitizing temperatures), depending on the maximum temperatures of thermal cycles.
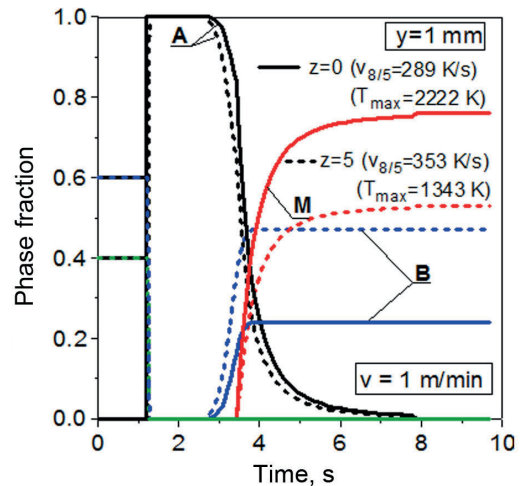

Fig. 7. Young's modulus, tangential modulus and yield strength assumed in simulations of mechanical phenomena, research 1 [39], research 2 [40]

Fig. 8. Kinetics of phase transformations at the top and bottom surfaces of welded joint

The analysis of phase transformations and the prediction of structural composition for welded joint is made on the basis of mathematical and numerical models taking into account the impact of most important parameters of thermal cycle on the kinetics of phase transformations in solid state. It is assumed on the basis of microscopic examination that the base structure (parent material) is a bainitic-ferritic structure, containing: 60% bainite and 40% ferrite.

Fig. 8 presents exemplary results of numerical simulations of the kinetics of phase transformations in welded joint at the distance y=1 mm from the centre of heat source activity zone, respectively for top surface and bottom surface of the joint (from the face and root of the weld). The kinetics of

Temperature distributions are presented in Fig. 9, in longitudinal section of the joint and for chosen material points in the cross section of the joint (y=0), along direction of material penetration. In Fig. 9b solidus, liquidus and boiling temperatures are marked as well as temperature range 800 and 500 °C where cooling rates are determined for analysis of phase transformations in solid state. Maximum temperatures are observed in the centre of heat source activity zone. At this point temperature exceeds the boiling point of steel (T_b), leading to the evaporation and creation of the keyhole.

Results of the prediction of structure composition in the cross section welded joint are shown in Fig. 10 as isolines of volumetric fractions of phases.
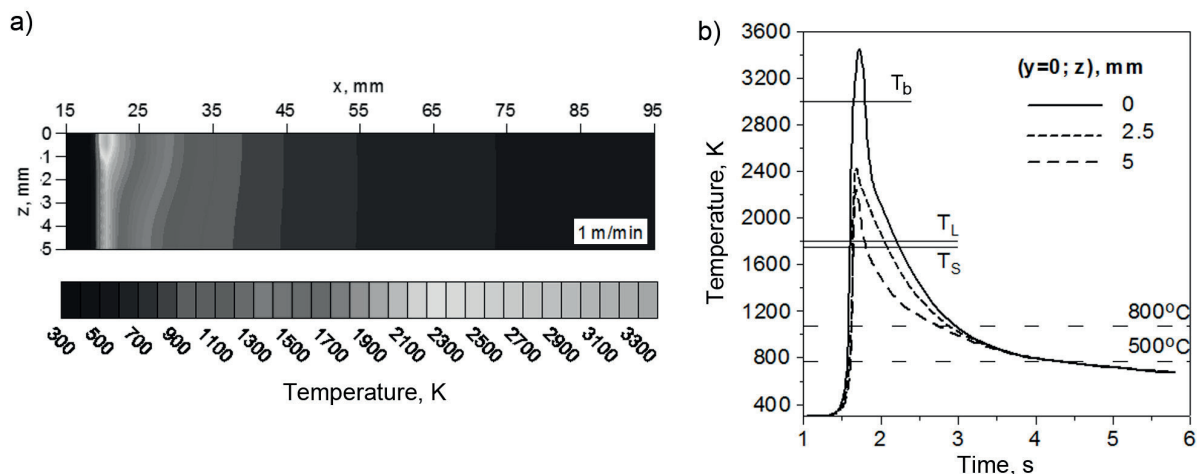

Fig. 9. Temperature distributions a) in the longitudinal section of the joint and b) for chosen points at different depths of the joint (for y=0)
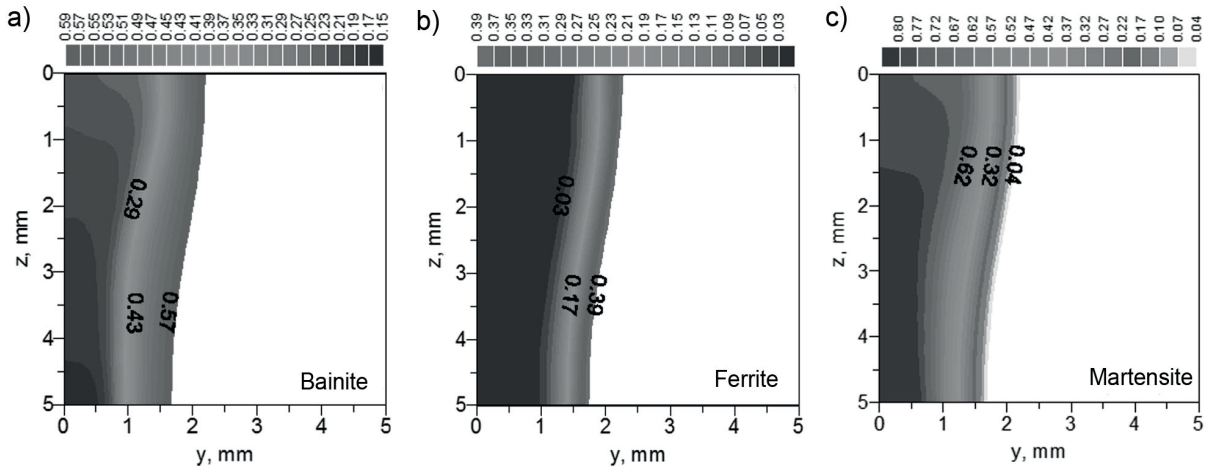
Fig. 10. Phase fractions of a) bainite, b) ferrite and c) martensite in the cross section of welded joint

Distributions of residual stresses after welding reflect the thermal load and structural deformations (the area of hardened structure, size of HAZ). Stress concentration occurs at the interface of HAZ with the base material. A significant fraction of hardening structures in welded joint indicates significant structural deformations and consequently occurring stresses. Normal stresses σ_x and σ_z are significant on the edge of the weld. Significant tension stresses also occur at the edge of the weld, which may lead to fractures from the root of welded joint (Figs 11 and 12).

Plasticizing zone (Fig. 13) reflects the zone of stress concentrations and significant plastic deformations are present only in the heat affected zone.
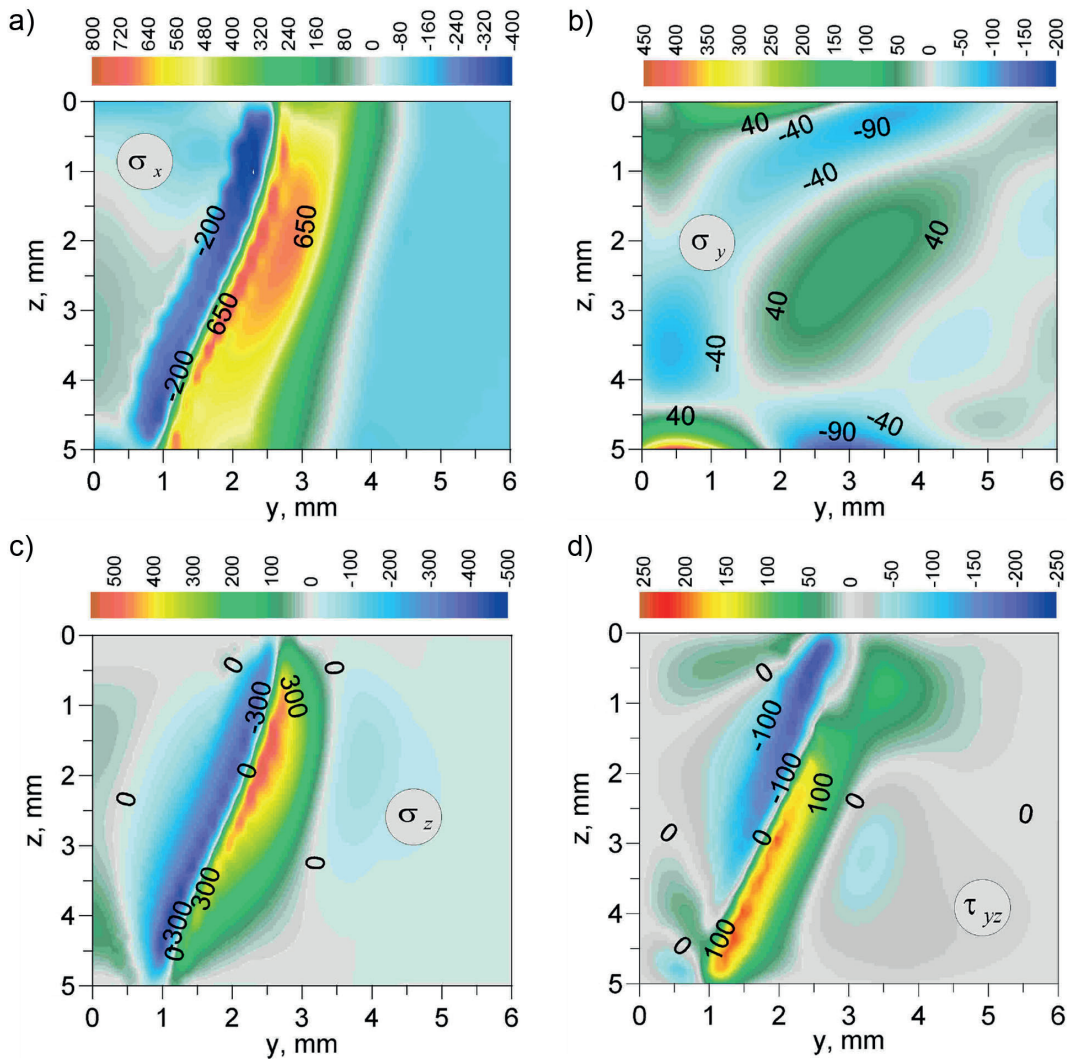

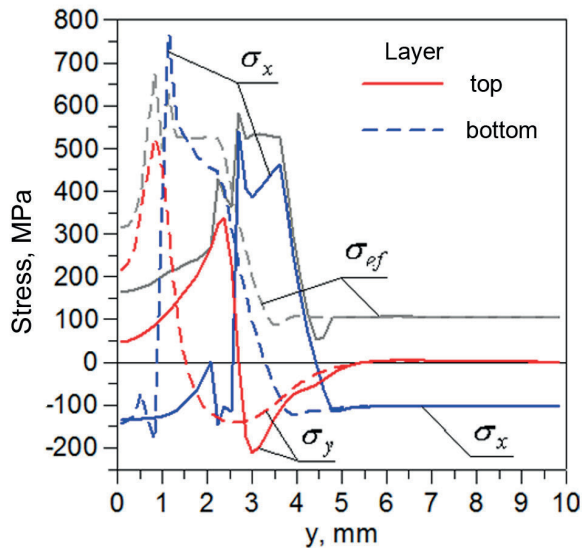Fig. 11. Distribution of residual stress in the cross section of welded joint

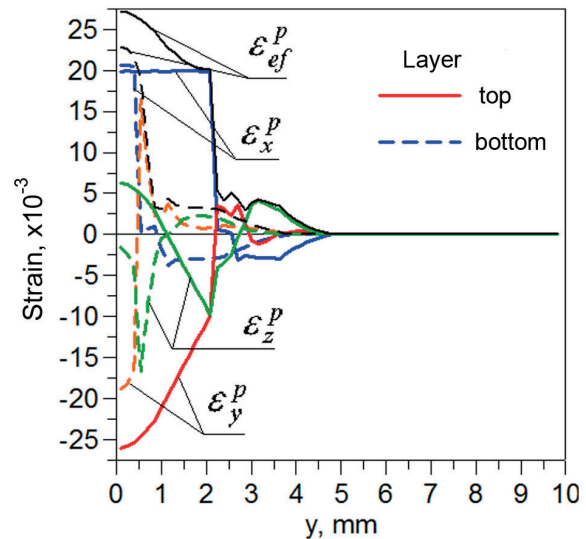Fig. 12. Residual stress in extreme layers of welded joint

Fig. 13. Distribution of plastic strain in extreme layers of welded joint

6. Final remarks

High heating and cooling rates and various maximum heating temperatures occur during welding using laser beam heat source. This requires a modified approach to numerical modeling of phase transformations in solid state. Good results are achieved through the use of "dynamic", discrete CCT diagrams. Numerically designated structural composition with corresponding to CCT diagrams phase composition of welded joint, together with the interpretation of hardness distribution in the joint proves the validity of this approach to the numerical modeling of laser welding process.

Distributions of stresses reflect thermal load and the load generated by structural strain. Stress concentration occurs at the interface of HAZ and the base material. A significant fraction of hardening structures in welded joint generates a structural deformation which causes significant stress. Significant normal stresses σ_x and σ_z occur as well as transverse tensile stresses at the edge of the weld, which may lead to fractures from the root of the weld. Significant plastic deformations occur only in the heat affected zone.

Presented numerical models allow for a comprehensive analysis of physical phenomena occurring during laser beam welding. This comprehensive approach allows for the analysis of laser beam welding performed for joints made of any type of steel and any thickness of welded elements.

REFERENCES

[1] Y.C. Kim, M. Hirohata, K. Inose, Welding in the World, no **3**, 64 (2012).

[2] T.L. Chen, Y.H. Guan, H.G. Wang, J.T. Zhang, J Mater Process Tech. **63**, 546 (1997).

[3] B. Chen, X.H. Peng, S.N. Nong, X.C. Liang, J Mater Process Tech. **122**, 208 (2002).

[4] A.P. Mackwood, R.C. Cafer, Opt Laser Technol. **37**, 99 (2005).

[5] D. Gery, H. Long, P. Maropoulos, J Mater Process Tech. **167**, 393 (2005).

[6] W. Zhang, B. Wood, T. DebRoy, et al., Acta Mater. **51**, 3333 (2003).

[7] W.S. Chang, S.J. Na, J Mater Process Tech. **120**, 208 (2002).

[8] H. Huang, J. Wang, L. Li, N. Ma, J Mater Process Tech. **227**, 117 (2016).

[9] W. Tan, Y.C. Shin, Comp Mater Sci. **98**, 446 (2015).

[10] A. Franco, L. Romoli, A. Musacchio, Int J Therm Sci. **79**, 194 (2014).

[11] F. Nagela, F. Simon, B. Kummel, J.P. Bergmanna, J. Hildebrand, Phys Proc. **56**, 1242 (2014).

[12] C. Garcia de Andres, F.G. Caballero, C. Capdevila, L.F. Alvarez, Materials Characterization, **48**, 101 (2002).

[13] S.A. Tsirkas, P. Papanikos, Th. Kermanidis, J Mater Process Tech. **134**, 59 (2003).

[14] K. Fanrong, M. Junjie, K. Radovan, J Mater Process Tech. **211**, 1102 (2011).

[15] W. Piekarska, Analiza numeryczna zjawisk termomechanicznych procesu spawania laserowego, Częstochowa, (2007).

[16] M.E. Le Guen, R. Fabbri, F. Coste, Ph. Le Masson, J Heat Mass Trans. **54**, 1313 (2011).

[17] N. Ma, L. Li, H. Huang, S. Chang, H. Murakawa, J Mater Process Tech. **220**, 36 (2015).

[18] L. Han, F.W. Liou, Int J Heat Mass Trans. **47**, 4385 (2004).

[19] X. Jin, L. Li, Y. Zhang, J Phys. D: Appl Phys. **35**, 2304 (2002).

[20] D.V Bedenko, O.B Kovalev, I.V. Krivtsun, J Phys D: Appl Phys. **43**, 1055 (2010).

[21] M. Beck, P. Berger, H. Hugel, J Phys D: Appl Phys. **28**, 2430 (1995).

[22] M. Dal, R. Fabbro, An overview of the state of art in laser welding simulation, Opt Laser Technol. (2015).

[23] W. Piekarska, M. Kubiak, Z. Saternus, Arch Metall Mater. **58** (4), 1391 (2013).

[24] J. Pilarczyk, M. Banasik, J. Stano, Przeglad Spawalnictwa, **5-6**, 6 (2006).

[25] C.F. Berkhout, P.H. van Lent, Schweißen und Schneiden. **6**, 256 (1968).

[26] M.H. Sorsorov, Fazovye prevrascenia i izmenenia svojstv stali pri svarke, isd. Nauka, Moskva, (1972).

[27] K. Röhrs, V. Michailow, H. Wohlfahrt, Proc. of Int. Conference Mathematical Modelling and Information Technologies in Welding and Related Processes, Katsiveli, Crimea, Ukraine, ed. V.I. Makhnenko, E.O. Paton Welding Inst. of NAS of Ukraine, Kiev, 92 (2002).

[28] J. Słania, Arch Metall Mater. **3**, 757 (2005).

[29] L. Taleb, F. Sidoroff, Int J Plasticity. **19**, 1821 (2003).

[30] A. Bokota, T. Domański, Arch Metall Mater. Issue 2, **52**, 277 (2007).

[31] M. Dalgic, G. Löwisch, Mat.-wiss. u. Werkstofftech. **37**, 1, 122 (2006).

[32] D.Y. Ju, W.M. Zhang, Y. Zhang, Mat Sci Eng A **438-440**, 246 (2006).

[33] K.J. Lee, Scripta Mater. **40**, 735 (1999).

[34] S. Serajzadeh, J Mater Process Tech. **146**, 311 (2004).

[35] W. Piekarska, M. Kubiak, A. Bokota, Arch Metall Mater. **56**, 409 (2011).

[36] M.J. Avrami; Chem. Phys., 7, 1103-1112 (1939) Atlas of Time –Temperature Diagrams for Irons and Steels, ed. V. Voort G. F., USA, ASM International, USA, (1991).

[37] D.P. Koistinen, R.E. Marburger, Acta Metall. **7**, 59 (1959).

[38] O.C. Zienkiewicz, R.L. Taylor, Butterworth-Heinemann, Fifth edition, vol. 1,2,3, (2000).

[39] V.I. Makhnenko, E.A. Velikoivanenko, O.V. Makhnenko, G.F. Rozynka, N.I., Avtomaticeskaja svarka. **5**, 3 (2000).

[40] M. Coret, A. Combescure, Int J Mech Sci. **44**, 1947 (2002).